# Revisiting spin ice physics in the ferromagnetic Ising pyrochlore $Pr_2Sn_2O_7$

Brenden R. Ortiz,[1,*] Paul M. Sarte,[2] Ganesh Pokharel,[2] Miles J. Knudtson,[2] Steven J. Gomez Alvarado,[2] Andrew F. May,[1] Stuart Calder,[3] Lucile Mangin-Thro,[4] Andrew R. Wildes,[4] Haidong Zhou,[5] Gabriele Sala,[6] Chris R. Wiebe,[7,8,9] Stephen D. Wilson,[2] Joseph A. M. Paddison,[1,†] and Adam A. Aczel[3,‡]

[1]*Materials Science and Technology Division, Oak Ridge National Laboratory, Oak Ridge, Tennessee 37831, USA*
[2]*Materials Department, University of California Santa Barbara, Santa Barbara, California 93106, USA*
[3]*Neutron Scattering Division, Oak Ridge National Laboratory, Oak Ridge, Tennessee 37831, USA*
[4]*Institut Laue-Langevin, 71 avenue des Martyrs, 38000 Grenoble, France*
[5]*Department of Physics and Astronomy, University of Tennessee, Knoxville, Tennessee 37996, USA*
[6]*Spallation Neutron Source, Second Target Station, Oak Ridge National Laboratory, Oak Ridge, Tennessee 37831, USA*
[7]*Department of Chemistry, University of Manitoba, Winnipeg, Manitoba, Canada R3T 2N2*
[8]*Department of Chemistry, University of Winnipeg, Winnipeg, Manitoba, Canada R3B 2E9*
[9]*Department of Physics and Astronomy, McMaster University, Hamilton, Ontario, Canada L8S 4M1*

(Received 24 October 2023; accepted 26 March 2024; published 15 April 2024)

Pyrochlore materials are characterized by their hallmark network of corner-sharing rare-earth tetrahedra, which can produce a wide array of complex magnetic ground states. Ferromagnetic Ising pyrochlores often obey the "two-in-two-out" spin ice rules, which can lead to a highly degenerate spin structure. Large moment systems, such as $Ho_2Ti_2O_7$ and $Dy_2Ti_2O_7$, tend to host a classical spin ice state with low-temperature spin freezing and emergent magnetic monopoles. Systems with smaller effective moments, such as $Pr^{3+}$-based pyrochlores, have been proposed as excellent candidates for hosting a "quantum spin ice" characterized by entanglement and a slew of exotic quasiparticle excitations. However, experimental evidence for a quantum spin ice state has remained elusive. Here, we show that the low-temperature magnetic properties of $Pr_2Sn_2O_7$ satisfy several important criteria for continued consideration as a quantum spin ice. We find that $Pr_2Sn_2O_7$ exhibits two distinct spin-correlation time scales of $\tau \geqslant 10^{-4}$ and $\sim 10^{-10}$ s in the spin ice regime. Our comprehensive bulk characterization and neutron scattering measurements enable us to map out the magnetic field-temperature phase diagram, producing results consistent with expectations for a ferromagnetic Ising pyrochlore. We identify key hallmarks of spin ice physics and show that the application of small magnetic fields ($\mu_0 H_c \sim 0.5$ T) suppresses the spin ice state and induces a field-polarized, ordered spin-ice phase. Together, our work clarifies the current state of $Pr_2Sn_2O_7$ and encourages future studies aimed at exploring the potential for a quantum spin ice ground state in this system.

DOI: 10.1103/PhysRevB.109.134420

## I. INTRODUCTION

Quantum spin liquids [1–9] and spin ices [10–14] are some of the exotic states of matter that arise from the interplay of magnetism on a frustrated lattice. In both cases, frustration impedes the ability to satisfy competing exchange interactions, producing a largely degenerate ground state and suppressing conventional magnetic order. Rare earth pyrochlores exhibit a frustrated lattice of corner-sharing tetrahedra decorated with rare earth ions and exhibit two different varieties of spin ice. Large moment systems such as $Dy_2Ti_2O_7$ and $Ho_2Ti_2O_7$ exhibit a classical spin ice (CSI) state, with well-isolated crystal field ground state doublets and nearly pure $|M_J = \pm J\rangle$ wave functions, where $J$ is the total angular momentum quantum number. Here, the spins on each tetrahedron obey the "two-in-two-out" ice rule and the thermal excitations behave as emergent magnetic charges [15]. The quantum spin ice (QSI) state [14,16,17], which is a particular type of quantum spin liquid, expands on this phenomenology and supports a system of emergent electrodynamics with different flavors of quasiparticles that resemble photons, electric charges, and magnetic charges. In principle, this novel state can be realized by adding quantum-tunneling terms arising from significant quantum fluctuations to the CSI model [18,19]. In practice, this requires terms in the magnetic Hamiltonian that couple components of the spins transverse to the Ising axis. Although well-isolated crystal field ground state doublets are still important for satisfying this criterion, the wave functions must now contain a significant admixture of terms $|M_J \neq \pm J\rangle$. Despite some success in identifying rare earth pyrochlores with the desired crystal field ground states, spin ice correlations, and significant quantum fluctuations, definitively establishing a QSI state in a real material has proven to be difficult [14,17]. The search for quantum analogs of ice therefore remains a key goal of condensed matter physics.

*ortizbr@ornl.gov
†paddisonja@ornl.gov
‡aczelaa@ornl.gov

 ©2024 American Physical Society

Pyrochlores based on $Pr^{3+}$ ions ($J = 4$) have been identified as intriguing QSI candidates. Of these, $Pr_2Zr_2O_7$ and $Pr_2Hf_2O_7$ have received the most attention due to the availability of large single crystals grown by the floating zone method [20–23]. The $Pr^{3+}$ crystal field ground states are non-Kramers doublets with Ising anisotropy [24–27] and they are well separated from the first excited crystal-field levels with large energy gaps of 9.5 meV and 9.1 meV for the Zr [24,25] and Hf [26,27] systems, respectively. Accordingly, a $J_{\text{eff}} = \frac{1}{2}$ pseudospin model can provide an appropriate description of the low-temperature magnetic properties. Evidence for spin ice correlations includes Pauling's residual entropy [24], pinch point scattering [24,28,29], and a metamagnetic transition to a kagome ice state when the applied magnetic field $\boldsymbol{H} \parallel [111]$ [27,30]. The observation of quasielastic magnetic neutron scattering below 1 K [24,27,29,31] combined with evidence for partial spin freezing [24,26–28,32] indicates that part of the spin system remains dynamic and therefore demonstrates the importance of quantum fluctuations for both materials [24,28,29,31].

Thus, the behavior in Pr-containing pyrochlores is very different from that of CSI systems such as $Ho_2Ti_2O_7$ and $Dy_2Ti_2O_7$, which show no measurable inelastic scattering in the same energy range [33] and have much longer spin correlation times at low temperature [34,35]. Key signatures of the QSI state, including suppressed pinch point scattering and an inelastic spin excitation continuum, have been identified in $Pr_2Hf_2O_7$ [29]. The unusual low-temperature heat conduction for $Pr_2Zr_2O_7$ has also been attributed to a QSI state, argued to arise from the different quasiparticles associated with it [36]. Unfortunately, most $Pr_2Zr_2O_7$ samples are known to be affected by structural disorder likely arising from Pr off-centering or $Pr^{4+}$ defects [21]. While there is currently no consensus if this disorder is strong enough to induce a paramagnetic state with quadrupolar correlations [28,37,38] or if a quantum spin liquid state is realized instead [31], recent success in synthesizing and characterizing pristine $Pr_2Zr_2O_7$ crystals suggests that the intrinsic ground state of this system is a QSI [30].

$Pr_2Sn_2O_7$ has also been put forth as a QSI candidate [39]. The $Pr^{3+}$ ions have a non-Kramers doublet ground state with an energy gap of 17.8 meV to the first excited state [39,40], which is significantly larger than for the Zr and Hf analogs. The powder-averaged magnetic diffuse scattering is reminiscent of expectations for CSI but not completely captured by this model, with improved agreement between theory and experiment obtained when considering an anisotropic exchange model with quantum fluctuations instead [41,42]. Commonalities with the other Pr-based pyrochlores include Ising moments [40], a small, positive Curie-Weiss temperature [39], and magnetic quasielastic neutron scattering below 1 K [39] that are typically seen as strong evidence for spin ice correlations and significant quantum fluctuations. Key differences between $Pr_2Sn_2O_7$ and the other Pr pyrochlores have also been identified. A residual entropy greater than Pauling's value was reported in $Pr_2Sn_2O_7$, which was partially suppressed by a 1 T applied magnetic field [39]. Previous ac susceptibility measurements have also shown evidence for full spin freezing [43], which is in line with expectations for CSI, but apparently inconsistent with related work on $Pr_2Sn_2O_7$ [39] and the other Pr pyrochlores, which generally support dynamical ground states with partial (or drastically suppressed) spin freezing signatures [24,27,28]. Another unique aspect of $Pr_2Sn_2O_7$ is the fine structure that was observed in its quasielastic neutron scattering spectrum [44]. This was explained by a magnetic monopole confinement model appropriate for QSI arising from a finite tension of the Dirac strings that connect monopole pairs [44], although the origin for the linear potential giving rise to the string tension is still unknown.

Despite the intriguing properties of $Pr_2Sn_2O_7$, the ongoing interest in QSI physics, and the notable discrepancies between some key properties of this material and the other Pr pyrochlores, subsequent investigations of $Pr_2Sn_2O_7$ have been conspicuously absent in the literature. We address this issue here by performing a series of comprehensive measurements aimed at characterizing the low-temperature magnetic properties of traditionally prepared samples of this QSI candidate. We confirm key spin-ice signatures including residual Pauling entropy. Using ac susceptibility measurements, we identify a partial spin-freezing signature around 0.25 K likely extrinsic in origin and a separate signal from a relatively slow spin-correlation time $\tau \geqslant 10^{-4}$ s below 0.5 K. Next, using our field-dependent measurements, we establish a $H$-$T$ phase diagram for $Pr_2Sn_2O_7$ that is consistent with a ferromagnetic Ising pyrochlore. We show that the spin ice state is extremely fragile, with a field-polarized ordered spin-ice phase achieved upon application of a modest magnetic field $\mu_0 H < 1$ T. Finally, using inelastic neutron scattering, we observe spin dynamics with a second, relatively fast, spin-correlation time $\tau \sim 10^{-10}$ s below 0.5 K. These results establish a partially frozen magnetic ground state for $Pr_2Sn_2O_7$ with a dynamic component consisting of two distinct spin correlation times. Our combined results show that $Pr_2Sn_2O_7$ is a spin ice system that should receive continued consideration as a potential host of an exotic QSI state.

## II. EXPERIMENTAL DETAILS

### A. Synthesis

Polycrystalline samples of $Pr_2Sn_2O_7$ were synthesized by the traditionally reported standard solid-state reaction using stoichiometric amounts of $Pr_6O_{11}$ (99.99%, Alfa Aesar) and $SnO_2$ (99.99%, Alfa Aesar). For consistency with prior literature methods, the powder reagents were mixed together and finely ground with a mortar and pestle. The resulting fine powder was placed in an alumina crucible and prereacted by heating in air at 1000 °C for 24 h. Samples were then reground and heated in air at 1400 °C for approximately 48 h with intermittent grindings until room temperature powder x-ray diffraction (XRD) measurements confirmed no discernible impurities. Phase purity was confirmed with room temperature XRD on a PANalytical X'Pert Pro MPD diffractometer (monochromated Cu $K_{\alpha 1}$ radiation) in standard Bragg-Brentano ($\theta$-$2\theta$) geometry. Rietveld refinements of the powder XRD patterns were performed using TOPAS ACADEMIC v6 [45]. Structural models and visualization utilized the VESTA software package [46].

### B. Magnetization and heat capacity measurements

Temperature and field-dependent dc magnetization measurements were performed on a 7 T Quantum Design (QD) Magnetic Property Measurement System (MPMS3) SQUID magnetometer in vibrating-sample (VSM) mode. Polycrystalline $Pr_2Sn_2O_7$ was placed in a polypropylene capsule and subsequently mounted in a brass holder. The temperature and field-dependent ac magnetization measurements were performed on a QD 9 T Dynacool Physical Property Measurement System (PPMS) employing the ac susceptibility option for the dilution fridge (ACDR). $Pr_2Sn_2O_7$ powder was cold pressed with a Carver press and a portion of the resulting pellet with approximate dimensions of $1 \times 1 \times 0.5$ mm$^3$ was adhered to a sapphire sample mounting post with a thin layer of Apiezon N-grease. Unless specified, all ac susceptibility measurements were collected under field-cooled (FC) conditions.

The heat capacity of $Pr_2Sn_2O_7$ and its corresponding nonmagnetic analog $La_2Sn_2O_7$ were measured with a QD 9 T Dynacool Physical Property Measurement System (PPMS) for both conventional $^4$He and dilution refrigerator temperature ranges. For the dilution fridge measurements, powder samples of $Pr_2Sn_2O_7$ and $La_2Sn_2O_7$ were blended with silver powder (Alfa Aesar, 99.999%) to aid in thermal coupling to the sample stage and a more accurate assessment of the nuclear Schottky anomaly in the 60–500 mK range. We endeavored to collect a high density of points in many of the magnetization and heat capacity measurements. In lieu of a binned average, we have opted to show the bulk of the data with a moving average over the nearest- and next-nearest neighbor points. This helps reduce measurement noise and does not introduce significant changes to any of the quantitative results presented in the manuscript.

### C. Neutron scattering

Neutron powder diffraction (NPD) measurements were performed on the high-resolution powder diffractometer HB-2A [47] of the High Flux Isotope Reactor (HFIR) at ORNL in applied magnetic fields up to 4 T and temperatures down to 1.6 K. For these measurements, $Pr_2Sn_2O_7$ powder was pressed with a Carver press into pellets which were loaded in a cylindrical Cu can. Diffraction data were collected with a neutron wavelength $\lambda_n$ of 2.41 Å and a collimation of open-21′-12′. Rietveld refinements were performed using the TOPAS ACADEMIC v6 software package and the magnetic structure symmetry analysis was performed using SARAH [48].

Polarized diffuse neutron scattering experiments were performed on the diffuse scattering spectrometer D7 [49] at the Institut Laue-Langevin (ILL). An incident wavelength of 4.8 Å was selected by a pyrolytic graphite monochromator. Data were collected in the absence of an external dc field and in non-time-of-flight mode, leading to the extraction of the energy-integrated scattering intensity between $-20 \leqslant E \leqslant 3.5$ meV. $Pr_2Sn_2O_7$ powder was loaded in a double-wall cylindrical Cu can under 1 atm of He gas and then placed in the dilution fridge insert of a cryostat with a base temperature of 0.05 K, when measured at the mixing chamber. Data were collected at 0.05, 1.0, and 50 K. Data normalization by a vanadium standard ensured that differences in detector efficiency and solid angle coverage were taken into account. Scattering contributions from an empty and a cadmium-filled sample holder were added together and weighted by the sample transmission to estimate the instrument background. Corrections for polarization efficiency of the supermirror analyzers were made by using the scattering from amorphous quartz. Equal counting times were spent on measuring the scattering along the $x$, $y$, and $z$ directions. The 6-pt $xyz$ polarization analysis method [50] was used to separate the magnetic, nuclear coherent, and nuclear-spin incoherent scattering channels for each wave vector transfer magnitude $Q$. The non-spin-flip and spin-flip scattering along each of the three directions were measured with a time ratio of 1:4. It has been shown that the 6-pt $xyz$ polarization analysis method becomes inaccurate at small $Q$, where a spurious transfer of intensity from the magnetic to the nuclear-spin incoherent channel occurs due to scattering away from the horizontal plane [51]. We performed an approximate correction for this effect by fitting the nuclear spin-incoherent channel at each temperature to the form $c + b/Q^2$, where $b$ and $c$ are fit parameters, and then obtaining the corrected magnetic scattering by adding the $b/Q^2$ term to the uncorrected magnetic scattering.

Low energy inelastic neutron scattering (INS) measurements were collected using the Disk Chopper Time-of-Flight Spectrometer (DCS) [52] at the National Institute of Standards and Technology (NIST) Center for Neutron Research (NCNR) in two separate experiments. $Pr_2Sn_2O_7$ powder was loaded in a 1.25-cm-diameter cylindrical Cu can under 1 atm of He gas and then placed in a dilution fridge insert of a cryomagnet achieving a base temperature of 0.2 K in experiment 1 and 0.02 K in experiment 2. Some data from Expt. 1 were previously published in Ref. [39]. Temperatures were measured at the mixing chamber and the sample temperature may be higher due to difficulty of thermalizing large masses of powder; indeed, as we will discuss, our results are consistent with the sample reaching a base temperature ∼0.5 K in these measurements. Data were collected at 0.2 and 0.5 K in Expt. 1 and at 0.02, 0.5, and 4.2 K in Expt. 2. An incident wavelength of 9 Å and low-resolution mode were chosen, corresponding to a flux of $\sim 2 \times 10^5$ neutrons/cm$^2$ s with an elastic line resolution (full width at half maximum) of approximately 0.018 meV and an accessible $Q$ range of [0.1, 1.3] Å$^{-1}$ in the elastic channel. The DCS data were corrected for neutron absorption by the sample.

## III. RESULTS AND DISCUSSION

### A. Bulk properties measurements

The pyrochlore lattice remains one of the hallmark platforms for exploring the combination of rare-earth magnetism and a structurally frustrated lattice. Figure 1(a) shows the crystal structure of $Pr_2Sn_2O_7$, highlighting the corner-sharing magnetic tetrahedra (dark blue). Formally, however, each cation in $Pr_2Sn_2O_7$ is coordinated by oxygen and the subsequent Pr–O polyhedra and Sn–O octahedra form an edge-sharing network. Pyrochlore oxides are often produced through the "shake and bake" method, where reagent powders are hand-ground together before repeated sintering at high temperatures. The samples produced in this manner exhibit

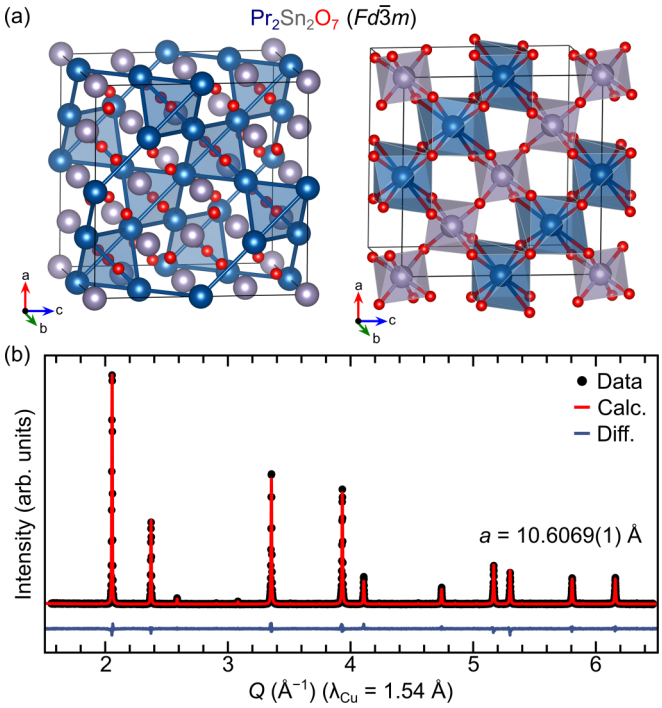


FIG. 1. (a) Crystal structure of $Pr_2Sn_2O_7$ shown in two perspectives. The left image highlights the rare-earth sublattice of corner-sharing tetrahedra. The right image depicts a slice through the structure, highlighting the edge-sharing network of Pr–O polyhedra and Sn–O octahedra. (b) Measured, calculated (Rietveld), and difference room temperature XRD profiles of polycrystalline $Pr_2Sn_2O_7$ collected at room temperature. Samples show excellent crystallinity with no detectable impurity phases.

excellent crystallinity and purity. We note that the powders have a light red-brown hue, which may suggest a small concentration of $Pr^{4+}$ defects. Informal discussion with the authors of Ref. [39] corroborate the coloration of polycrystalline samples. $Pr^{3+}$ oxides and $Pr^{4+}$ oxides are typically green and red in color, respectively, with mixed Pr valence systems taking on darker shades in some cases. It has been shown that the color of floating-zone grown $Pr_2Zr_2O_7$ crystals changes from dark brown to green as $Pr^{4+}$ defects are suppressed during growth [21]. Figure 1(b) presents the x-ray diffraction pattern for a representative $Pr_2Sn_2O_7$ powder sample, with the Rietveld refinement superimposed on the data. There are no discernible impurity peaks in the pattern and the lattice constant $a = 10.6069(1)$ Å agrees well with previous work [39,53–55]. Occupancies for Pr and Sn were refined, but did not deviate substantially from unity and were subsequently fixed.

In general, the magnetic properties of pyrochlores with non-Kramers crystal field doublets at the rare earth sites have shown remarkable sensitivity to chemical disorder, crystalline defects, and synthetic processes [3,21,24,30,38]. The potential for mixed valence defects is particularly prevalent in Pr-containing compounds, as nonmagnetic $Pr^{4+}$ can be disruptive to potentially fragile magnetic ground states. Previous work on polycrystalline $Pr_2Sn_2O_7$ highlights the importance of sample dependence, as Ref. [39] identifies quasielastic scattering that is typically associated with the enhanced low-temperature magnetic monopole density expected for a QSI state [14], while Ref. [43] presents ac susceptibility data that is more consistent with a CSI state that freezes completely. Since these studies focus on different measurements, direct comparisons between the two samples cannot be made. To provide a comprehensive examination of the properties of polycrystalline $Pr_2Sn_2O_7$ produced by standard solid-state methods, our manuscript examines a full suite of magnetic, thermodynamic, and neutron scattering measurements on traditionally prepared samples.

Figure 2(a) depicts the magnetization $M$ measured as a function of applied field $\mu_0 H$ at selected temperatures. The 1.8 K isothermal magnetization was fit using the powder-averaged expression for $J_{\text{eff}} = \frac{1}{2}$ Ising pyrochlores with $g = g_{\parallel}$:

$$\langle \mu \rangle / \mu_{\text{B}} = \frac{(k_B T)^2}{g \mu_{\text{B}} H^2 J_{\text{eff}}} \int_0^{g\mu_{\text{B}} H J_{\text{eff}}/k_B T} x \tanh(x)\, dx, \quad (1)$$

where $\mu_B$ is the Bohr magneton and $k_B$ is the Boltzmann constant. This expression accounts for systems where substantial single ion anisotropy prevents a more facile analysis using the free-ion Brillouin function. A more in-depth derivation of Eq. (1) can be found in Ref. [56]. The fitting result, which is overplotted on the 1.8 K data in Fig. 2(a), returns a $g_{\parallel}$ ($= g_{zz}$) value of 5.6(1). Figure 2(b) depicts the dc magnetization for $Pr_2Sn_2O_7$ as a function of temperature and magnetic field. While the low-field data ($\mu_0 H < 2.5$ T) exhibits Curie-Weiss temperature dependence down to 1.8 K, higher-field measurements feature an inflection point in the data that is indicative of a magnetic transition or crossover to a ground state with a net moment.

To provide a complete picture of the temperature-dependent magnetization, Fig. 2(c) overlays the low-field (0.01 T) dc susceptibility data (1.8–300 K) with the real component $\chi'(T)$ of the ac susceptibility (60 mK–4 K). The inset shows the linear behavior of the inverse dc susceptibility data in the temperature range 3–20 K, which was fit to a Curie-Weiss law to extract an effective moment 2.9(2) $\mu_{\text{B}}/Pr^{3+}$ and the ferromagnetic Curie-Weiss temperature 0.1(1) K. Both values are in good agreement with other studies [39,55]. We note that the results presented here agree favorably with predictions based on the experimentally measured crystal field levels (e.g., Ref. [40]). We also show a set of zero-field-cooled (ZFC) and field-cooled (FC) measurements for a high-frequency (10 kHz) ac susceptibility curve under a small (0.05 T) field. The onset of a slight splitting in the FC/ZFC curves is noted, coinciding with the primary peak in the susceptibility. This could suggest a minor contribution from a potentially glassy phase, such that the field history should be taken into consideration. Unless explicitly noted, all further thermodynamic measurements in this manuscript are performed in field-cooled conditions.

The absolute units for $\chi'$ were obtained by normalizing $\chi'(T)$ for each frequency to the dc susceptibility, by refining a vertical scale factor and offset such that the sum of squared differences between $\chi'(T)$ and the dc susceptibility was minimized over the temperature range $1.8 \leqslant T \leqslant 4$ K. Normalization is unavoidable due to the background inherent in the ac measurements in a dilution refrigerator. The assumption

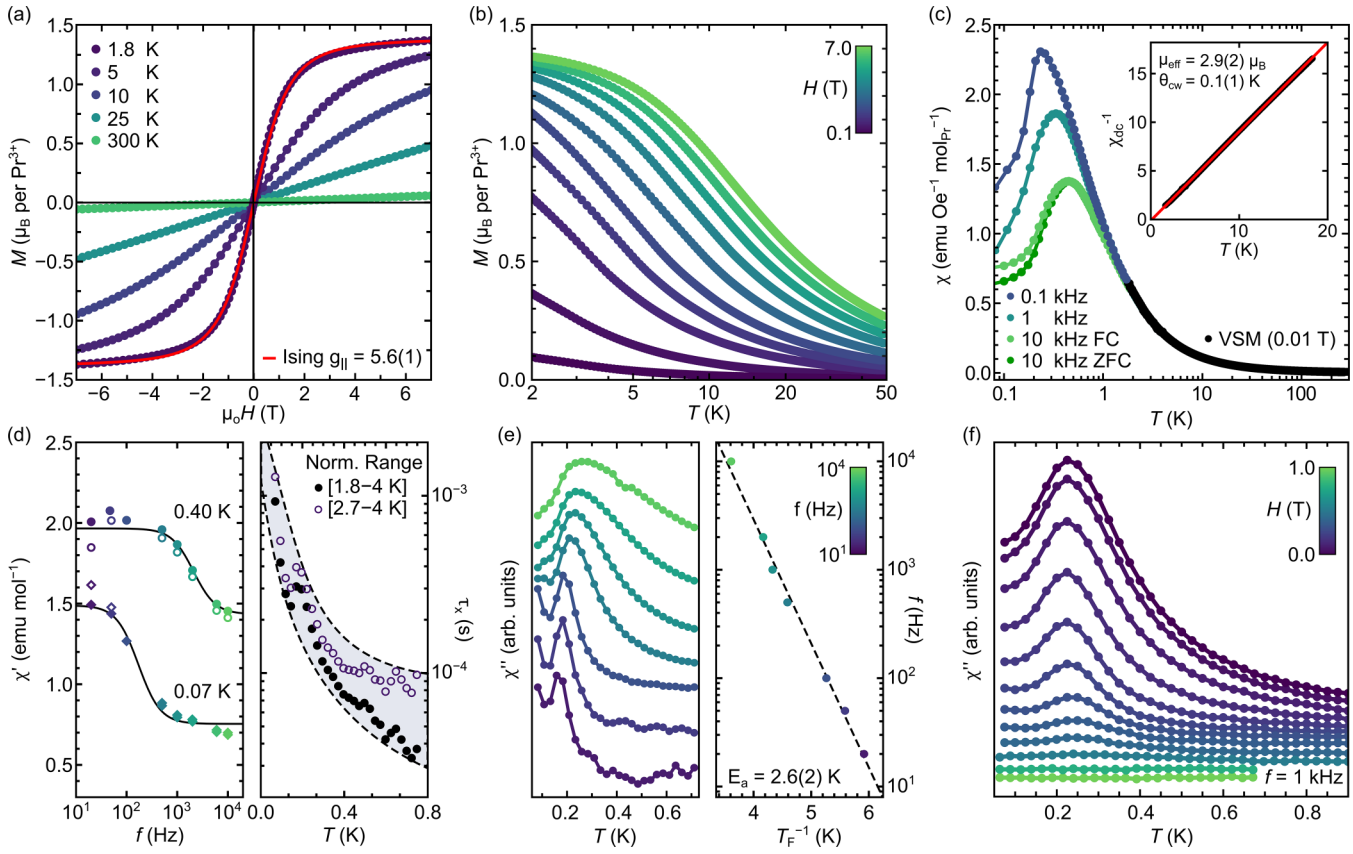


FIG. 2. (a) Field dependence of the isothermal magnetization data with the best fit to the powder-averaged $J_{\text{eff}} = \frac{1}{2}$ Ising model ($g_\perp = 0$) superimposed on the 1.8 K data. (b) dc (VSM) magnetization measurements as a function of magnetic field. The derivative $dM/dH$ was used to extract the characteristic field for the onset of the field-induced order. (c) Temperature dependence of the dc susceptibility and the ac susceptibility at selected frequencies and measurement conditions. The inset shows the Curie-Weiss analysis (fit from 3 K to 20 K) of the dc susceptibility data, which suggests the presence of weak net ferromagnetic exchange. (d) Frequency dependence of the real part of the ac susceptibility $\chi'$ for various temperatures in the absence of an external dc field (left, points), fits to the model described in the text (left, lines), and extracted spin correlation times as a function of temperature (right). Filled and hollow points show results obtained from $\chi'$ data normalized to dc data over different temperature ranges. (e) Temperature dependence of the imaginary part of the ac susceptibility $\chi''$ for various frequencies in the absence of an external dc field (left) and the corresponding Arrhenius fit of the freezing transition (right), which yields an activation energy $E_a = 2.6$ K. (f) Field dependence of the freezing transition in $\chi''$ using an intermediate driving frequency $f = 1$ kHz.

that $\chi'$ should equal the dc susceptibility holds in the paramagnetic regime, where the spin relaxation rate is much faster than the driving frequency [57]. There are two features of note in the low-temperature data: (1) an onset of partial spin freezing around 0.2–0.4 K indicated by a frequency-dependent peak in $\chi'(T)$ and (2) incomplete freezing as $T \to 0$. The onset of spin freezing was identified in $Pr_2Sn_2O_7$ previously [43] and is known in other CSI systems [58,59]. However, samples in Ref. [43] exhibit full spin freezing over all frequencies, where $\chi' \to 0$ as $T \to 0$. Our samples exhibit a partially frozen state, which is more consistent with recent results in other Pr pyrochlores [24,27,28]. It has been suggested that complete spin freezing, which has also been identified in a sample of $Pr_2Hf_2O_7$ [26], is extrinsic in origin. The wide sample dependence in $Pr^{3+}$-based pyrochlores speaks to the defect sensitivity of the materials and one possibility is that the spin freezing is nucleated by defects and/or disorder. We suspect that the low-temperature ac susceptibility spin-freezing signature should be suppressed in pristine samples. While a future goal will be to explore the defect energetics within $Pr_2Sn_2O_7$, our current manuscript is designed to clarify the state of traditionally prepared $Pr_2Sn_2O_7$ powders.

To obtain information about the spin-correlation time scales at low temperatures, we consider the frequency dependence of $\chi'$. Representative plots of $\chi'(f)$ at 0.07 and 0.40 K are shown in Fig. 2(d), left. To model these data, we employ the damped-harmonic oscillator model [57],

$$\chi'(f) = \chi_S + \frac{\chi_T - \chi_S}{1 + (2\pi f \tau)^2}, \tag{2}$$

where $f$ is the driving frequency, $\tau$ is the characteristic spin-correlation time, $\chi_S$ is the adiabatic susceptibility, and $\chi_T$ is the isothermal susceptibility. This model is equivalent to that employed for the quantum spin-ice candidate $Yb_2Ti_2O_7$ [60]. Figure 2(d), right, shows the temperature dependence of $\tau$ obtained from fits of $\tau$, $\chi_S$, and $\chi_T$ to the $\chi'(f)$ data at each temperature. The spin correlation time decreases from ∼1 ms at 0.07 K to ∼0.1 ms at 0.4 K. These values

should be interpreted as order-of-magnitude estimates due to systematic uncertainties in the data normalization; to estimate these uncertainties we show results from fits to $\chi'$ data normalized over two temperature ranges. Notably, these time scales are three orders of magnitude faster than for the classical spin ice $Dy_2Ti_2O_7$ [59]. At higher temperatures, the spin correlation time is too short to determine reliably using our ac data, which are insensitive to $\tau \lesssim 0.01$ ms. We will extend our analysis to shorter spin correlation times using neutron-scattering data in Sec. III D.

The temperature dependence of the imaginary part of the ac susceptibility $\chi''(T)$ for frequencies between 10 and $10^4$ Hz is shown in Fig. 2(e), with the freezing transition $T_f$ indicative of slow dynamics defined as the temperature corresponding to the signal's maximum value. The low-frequency value of $T_f = 0.17$ K is significantly suppressed compared to the 1 K energy scale for CSI [58,59]. The frequency dependence of $T_f$ is well described by the Arrhenius law $f = f_0 e^{-E_A/T_f}$, with slightly smaller $E_A$ and $f_0$ values of 2.6(2) K and 110(10) MHz as compared to previous work [43]. We present the field dependence of $\chi''$ using an intermediate frequency of 1 kHz in Fig. 2(f), where we find that the freezing transition temperature is largely unaffected by the application of modest fields. However, the strength of the peak in $\chi''$ diminishes sharply after $\mu_0 H \geqslant 0.5$ T and is difficult to distinguish above noise by 0.75 T. As such, we consider 0.5 T as a conservative lower bound for the critical field in polycrystalline $Pr_2Sn_2O_7$. Note that in Figs. 2(e) and 2(f) the curves are plotted to scale, although they have been vertically offset for clarity.

### B. Heat capacity

Next, we revisit the heat capacity of $Pr_2Sn_2O_7$ by collecting data down to dilution-refrigerator temperatures in both zero and applied magnetic fields. Our measurements are motivated by two main factors. First, a careful analysis of the nuclear Schottky anomaly contribution can help to constrain the spin correlation time associated with the magnetic ground state of the system. Secondly, an entropy analysis that includes lower temperature data may help to resolve a longstanding puzzle in the literature: previous heat capacity work reports a zero-field entropy that falls substantially short of Pauling's value for a classical spin ice state [39]. This result is seemingly at odds with the near-complete spin freezing observed in earlier ac susceptibility measurements [43] and previous work on the zirconate analog $Pr_2Zr_2O_7$ [24]. However, it is important to note that the data set in [39] is limited to 0.4 K, which will only capture a small (and heavily convoluted) part of the nuclear Schottky anomaly. As we will see, careful subtraction of the nuclear component can help alleviate these inconsistencies.

Figure 3(a) presents heat capacity data ($C_{\text{p,tot}}$) for traditionally prepared, polycrystalline $Pr_2Sn_2O_7$ at selected fields. The red solid curve highlights the lattice contribution to the specific heat, approximated using the nonmagnetic analog $La_2Sn_2O_7$. Figure 3(b) shows the same data but now with the lattice contribution subtracted, so only the nuclear and magnetic components are remaining ($C_{\text{p,nm}}$). As best observed in Fig. 3(c), there are two principal features in the $C_{\text{p,nm}}$ zero-field data: a broad peak centered around 1 K and a sharper peak close to the base temperature of 60 mK. This two peak structure is also visible in the finite field data, with both peak positions displaying significant field dependence. The higher-temperature peak signifies the development of spin ice correlations or a transition (crossover) from a paramagnetic to a long-range ordered (field-polarized) ground state in the low- and high-field regimes, respectively. The low-temperature peak has a nuclear Schottky origin, which must be subtracted off from the $C_{\text{p,nm}}$ data to obtain a reliable estimate for the magnetic entropy release of this system.

In general, a Schottky anomaly manifests when there is a system where particles can exist in $m$ energy levels, separated from the ground state by the associated energies $\epsilon_1, \epsilon_2, \ldots, \epsilon_m$ with degeneracies $g_1, g_2, \ldots, g_m$. A statistical approach using the Boltzmann factor can be used to drive the specific heat of a system of $N$ particles at an effective temperature $T$ [61]:

$$C_n = \frac{d}{dT}\left[\frac{N\sum_{r=0}^{m}\epsilon_r g_r e^{-\epsilon_r/kT}}{\sum_{r=0}^{m} g_r e^{-\epsilon_r/kT}}\right]. \tag{3}$$

Note that, while the magnetic field is not contained explicitly within Eq. (3), for the special case of a nuclear Schottky anomaly it generates a splitting of the nuclear energy levels that gives rise to the associated energies $\epsilon_1, \epsilon_2, \ldots, \epsilon_m$. There are several types of assumptions that can be made to evaluate the temperature dependence of the nuclear Schottky heat capacity. The most trivial approach is to assume a power series expansion of the specific heat; keeping the first term yields $C_n \propto T^{-2}$. This has been applied in many $Pr^{3+}$-based systems and works best when only the tail of the nuclear Schottky anomaly is captured or when the majority of the magnetic contribution is well separated from the nuclear contribution [26,62–66]. The second approximation is to assume a multilevel system with evenly spaced energy levels [61,66–71]. Here, $\epsilon_i = i \times \epsilon_0$, where $\epsilon_0$ is the characteristic energy splitting. This approach allows Eq. (3) to be evaluated numerically and is relatively flexible. A common simplification of this form is the application of a two-level system ($m = 1$, $\epsilon_i \in 0, \epsilon_1$). The most general approach would be to use the exact $\epsilon_i$ values derived either from spectroscopic or theoretical approaches, though there is often difficulty generalizing these results, particularly if magnetic fields are involved [68,72].

Another approach of note is the method utilized by Kimura *et al.* in their analysis of $Pr_2Zr_2O_7$ [24], with direct applicability to our data on $Pr_2Sn_2O_7$. They obtained the following expression for the Pr nuclear spin contribution to the specific heat arising from hyperfine dipole field splitting of the nuclear spin multiplet due to frozen Pr electronic moments [24]:

$$C_n = \frac{Nk_B\alpha^2}{4I^2}\left[\frac{1}{\sinh^2(\alpha/2I)} - \frac{(2I+1)^2}{\sinh^2[(2I+1)\alpha/2I]}\right], \tag{4}$$

where $\alpha = A_{\text{hf}}\mu_{\text{hyp}}^{\text{Pr}} I/g_J k_B T$, $N$ is Avogadro's number, $I = 5/2$ and $A_{\text{hf}}$ ($\approx 0.8$ T) are the nuclear spin and hyperfine coupling constant for $^{141}$Pr [73,74], and $g_J = 4/5$ and $\mu_{\text{Hyp}}^{\text{Pr}}$ are respectively the Landé $g$ factor and static magnetic dipole moment for $Pr^{3+}$. One advantage of this methodology is the comparison of the absolute magnitude of the observed Schottky anomaly with the theoretical prediction. In $Pr_2Zr_2O_7$, calculations based on the full ground state $Pr^{3+}$ doublet predict a large Schottky peak of $\sim$7 J/mol K. Experimentally, both

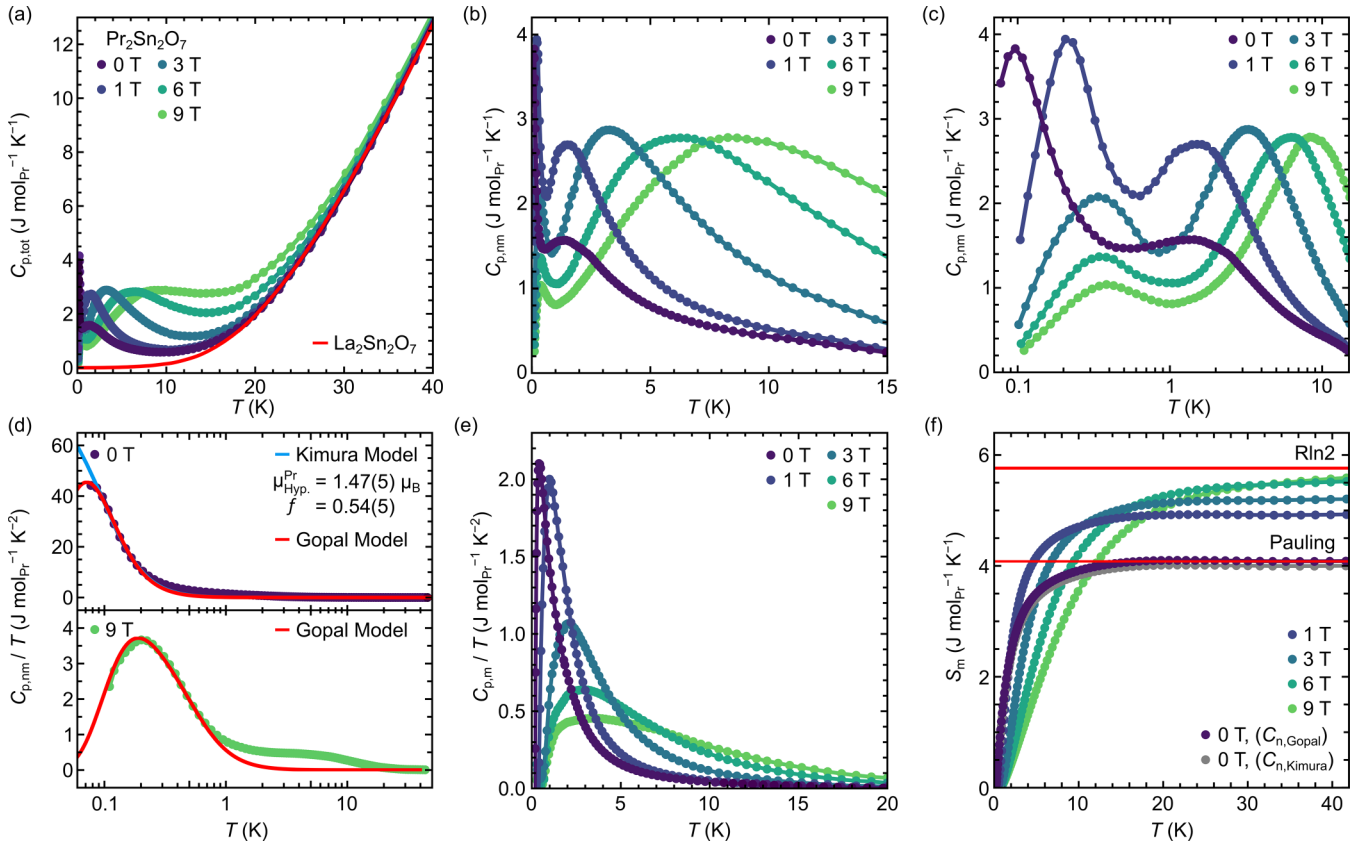


FIG. 3. (a) Heat capacity data for polycrystalline $Pr_2Sn_2O_7$ at selected magnetic fields. The lattice contribution from nonmagnetic $La_2Sn_2O_7$ is indicated by a solid red curve. (b) The lattice-subtracted specific heat as a function of field demonstrates a low-temperature nuclear Schottky anomaly and a higher temperature peak. (c) The same data shown in (b), but now presented using an $x$-axis log scale to emphasize the two distinct features observed for a given field. (d) Modeling of the nuclear Schottky anomaly using two different models: (1) an analytic form from Kimura *et al.* [24] for $Pr_2Zr_2O_7$ and (2) a generalized statistical-mechanical model provided by Gopal *et al.* [61]. (e) The magnetic component of $C_{p,m}/T$ after removal of the nuclear component. (f) Integration of the magnetic heat capacity provides insight into magnetic ground state. Regardless of the choice of nuclear Schottky model, at zero field we recover the full Pauling entropy, consistent with a spin-ice ground state. At the highest magnetic fields measured here, we nearly recover the full $R\ln(2)$ expected for a well-isolated crystal field ground state doublet.

$Pr_2Sn_2O_7$ (this work, Fig. 3) and $Pr_2Zr_2O_7$ (2–3 J/mol K) exhibit peaks substantially smaller than the theoretical limit [24]. Kimura *et al.* interpreted this result as signifying that a significant fraction of the Pr sites are not static on the nuclear hyperfine interaction time scale ($\tau > 1$) ns [24,75].

For our analysis, we did the following: (1) fit the expression derived by Kimura *et al.* to the zero-field $C_{\mathrm{p,nm}}$ data for direct comparison and (2) fit the generalized form given by Gopal *et al.* in Eq. (3) to both the zero-field and finite field data under the assumption that the energy levels split evenly (i.e., $\epsilon_i = i \times \epsilon_0$). The limiting cases of 0 T and 9 T are clearest. The low-field limit is expected to approach that of a two-level fit and the high 9 T field should be sufficient to fully split adjacent levels. The energy splitting was determined empirically using a least-squares fit to the data. We stress that these approaches are still approximations. However, we ultimately show that both approaches yield consistent results, despite their substantial differences.

Figure 3(d) shows the results of the nuclear Schottky modeling for both the 0 T (top) and 9 T (bottom) data sets. To highlight the Schottky contribution, results are shown in terms of $C_{\mathrm{p,nm}}/T$. For the 0 T data, the results based on Kimura (blue) and Gopal's methods (red) are both shown. There is a small discrepancy between the two models as $T \to 0$ K, but they agree remarkably well for the majority of the temperature range considered here. Presuming that the lowest temperature data points are dominated by the nuclear Schottky contribution (and are thus excluded from the Kimura model), both models should yield similar results. The extracted hyperfine moment and the phenomenological scale parameter $f$ are shown on the plot. The magnitude of the nuclear Schottky peak for our $Pr_2Sn_2O_7$ samples is approximately 3.8 J/mol K, which falls short of the predicted 7.06 J/mol K Schottky peak for a frozen spin system with the full crystal field moment of 2.6 $\mu_B$ [40]. The best fit yields $\mu_{\mathrm{hyp}}^{\mathrm{Pr}} = 1.47(5)\,\mu_B$ and $f = 0.54(5)$. A brief discussion by Kimura *et al.* around Eq. (4) suggested that deviations from the expected values could arise from sample inhomogeneity and/or low-lying electronic spin fluctuations. Our results for polycrystalline $Pr_2Sn_2O_7$ [$f = 0.54(5)$, $\mu_{\mathrm{hyp}}^{\mathrm{Pr}} = 1.47(5)\,\mu_B$] mimic those of $Pr_2Zr_2O_7$ [$f = 0.37$, $\mu_{\mathrm{hyp}}^{\mathrm{Pr}} = 0.82\,\mu_B$] [24,30], though $Pr_2Sn_2O_7$ lies closer to the completely frozen spin system limit.

Subtracting the nuclear contributions from the various data sets collected at fixed fields yields the magnetic heat capacity $C_m$, which is shown in Fig. 3(e) as $C_{p,m}/T$. The subtracted data contain smooth, broad magnetic peaks. Integrating the magnetic heat capacity yields the magnetic entropy $S_m$, shown in Fig. 3(f). Remarkably, we find that the zero-field data recovers the Pauling spin-ice entropy and does not depend substantially on the chosen nuclear Schottky model. The application of magnetic fields up to 9 T increases the recovered entropy and appears to approach the expected $R\ln(2)$ for a well-isolated crystal field ground state doublet. These results are similar to the findings in defect-rich [24] and pristine [30] $Pr_2Zr_2O_7$ single crystals, which both also host magnetic ground states with residual Pauling entropy.

### C. High-field neutron diffraction

To characterize the high-field magnetic ground state inferred from our bulk characterization measurements, we collected high-resolution diffraction patterns at temperatures $T \geqslant 1.6$ K in selected applied fields using HB-2A. The 0 T and 4 T data collected at 1.6 K are shown in Fig. 4(a). While the 0 T data refined well using a single phase for the sample corresponding to the expected pyrochlore crystal structure shown in Fig. 4(b), the 4 T data included enhanced intensity at $\boldsymbol{k} = \boldsymbol{0}$ positions and therefore different magnetic models were considered that could account for this additional signal.

Symmetry analysis using SARAH [48] identified four irreducible representations (IRs) given by $\Gamma_3$, $\Gamma_5$, $\Gamma_7$, and $\Gamma_9$ in Kovalev's notation [76], with detailed information about the possible spin configurations for each IR presented elsewhere [77]. The presence of a strong (002) magnetic Bragg peak at $Q = 1.19$ Å$^{-1}$ immediately rules out the $\Gamma_3$ and $\Gamma_5$ models since they do not generate magnetic intensity at this location. While the $\Gamma_7$ model does have a (002) magnetic Bragg peak in its diffraction pattern, the spin structure is antiferromagnetic and this is incompatible with the net moment for the field-induced phase observed in the susceptibility measurements. This leaves the $\Gamma_9$ model as the only viable candidate that is consistent with both the neutron powder diffraction and the magnetic susceptibility results. Indeed, the magnetic intensity in the 4 T diffraction pattern presented in Fig. 4(a) was captured well by a $\Gamma_9$ magnetic structure. The $\Gamma_9$ IR consists of two basis vectors $\psi_1$ and $\psi_2$ that correspond to moments lying parallel and perpendicular to the local $\langle 111 \rangle$ directions, respectively, with superpositions of them giving rise to intermediate moment directions. Notably, the model that generates the lowest agreement factor $R_{mag}$ with the 4 T $Pr_2Sn_2O_7$ data consists of a finite contribution for $\psi_1$ only and an ordered moment of 2.33(4) $\mu_B$.

This result agrees relatively well with the value of the crystal field moment associated with the non-Kramers ground state doublet (2.6 $\mu_B$ [40]) and the effective moment extracted from the low-temperature susceptibility presented in this work [2.9(2) $\mu_B$]. The magnetic structure corresponds to the ordered spin ice phase (No. 141.557, $I4_1/am'd'$), as shown in Fig. 4(b), where all the tetrahedra in the system satisfy the same ice rule. An identical spin configuration is induced by an applied magnetic field $\boldsymbol{H} \parallel [001]$ in both ferromagnetic and antiferromagnetic Ising pyrochlores, including $Dy_2Ti_2O_7$ [78,79], $Ho_2Ti_2O_7$ [79], $Tb_2Sn_2O_7$ [80], and $Nd_2Ir_2O_7$ [81]. A zero-field ordered spin ice state has also been identified in pyrochlores with two magnetic sites such as $Nd_2Mo_2O_7$ [82] and $Sm_2Mo_2O_7$ [83]. A field-induced canted version of this phase has been observed in polycrystalline $Nd_2GaSbO_7$ [84] and has been suggested in polycrystalline $Nd_2InSbO_7$ [85]. The ordered spin-ice phase for $Pr_2Sn_2O_7$ is likely generated by a combination of the applied magnetic field and Ising anisotropy, with exchange interactions not playing a significant role, and is hereby referred to as a "field-polarized phase."

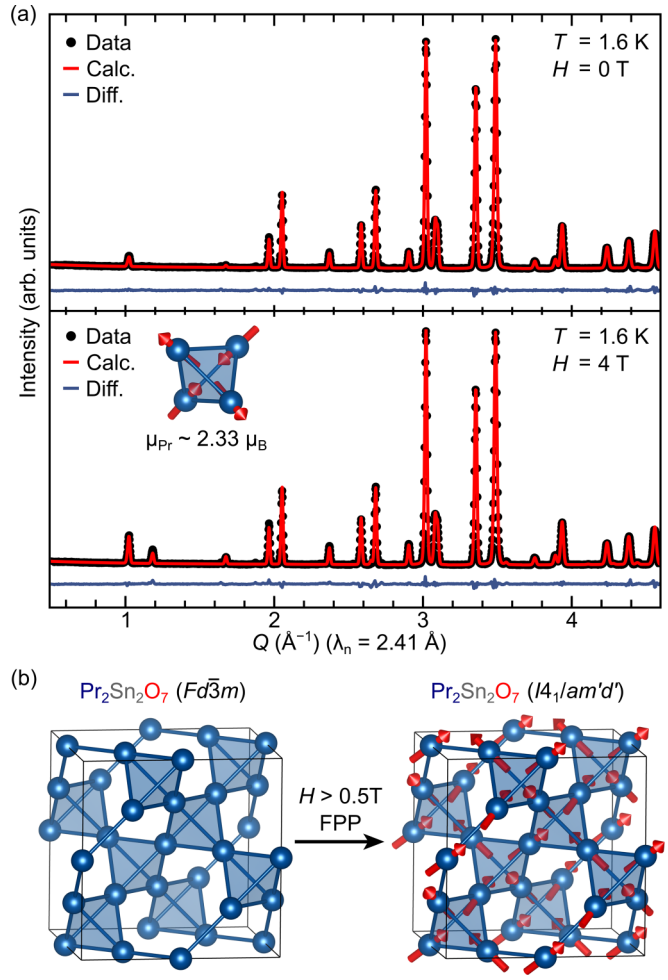


FIG. 4. (a) Measured, calculated (Rietveld), and difference neutron powder diffraction profiles ($T = 1.6$ K, $\lambda_n = 2.41$ Å) of polycrystalline $Pr_2Sn_2O_7$ in both the absence and presence of an external dc magnetic field. Contributions from the Bragg reflections of the sample container were fit using a Pawley refinement. Magnetic intensity appears in the 4 T data at $\boldsymbol{k} = \boldsymbol{0}$ Bragg positions. (b) The parent crystal structure of $Pr_2Sn_2O_7$ (left) and the field-induced ordered spin ice magnetic structure (right) showing only the Pr atoms for clarity.

Figure 5 summarizes the bulk characterization and HB-2A powder diffraction results for $Pr_2Sn_2O_7$ in a field-temperature phase diagram, with the different states labeled as spin ice (SI), field-polarized phase (FPP), and paramagnetic (PM) phase. The phase boundaries (or crossover region from FPP to PM) from the heat capacity ($^4$He $C_p$ and DR $C_p$) and dc susceptibility data ($^4$He $\chi_{dc}$) were determined by the higher-

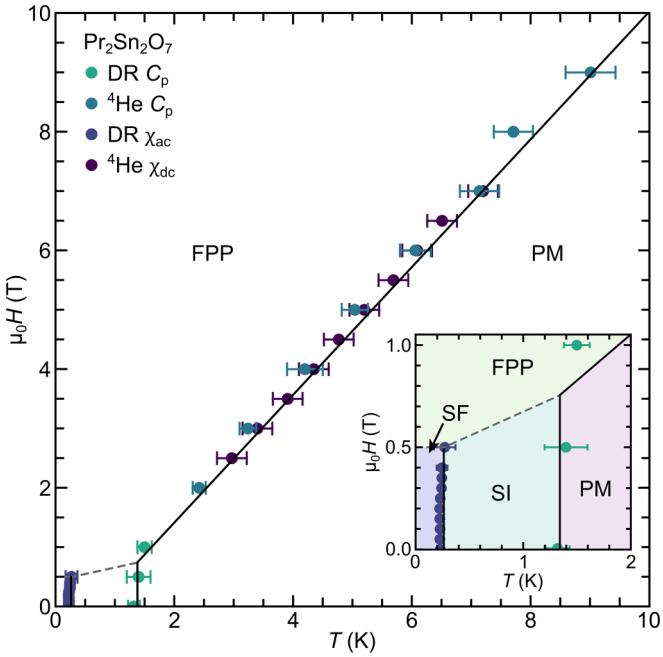


FIG. 5. Field-temperature phase diagram of $Pr_2Sn_2O_7$ as determined by heat capacity (DR $C_p$ and $^4$He $C_p$), ac susceptibility (DR $\chi_{ac}$), and dc susceptibility ($^4$He $\chi_{dc}$). Regions include a high-temperature paramagnetic (PM) state, field-polarized phase (FPP), spin ice (SI), and partial spin freezing (SF). The inset depicts an enlarged version of the low-temperature, low-field portion of the phase diagram.

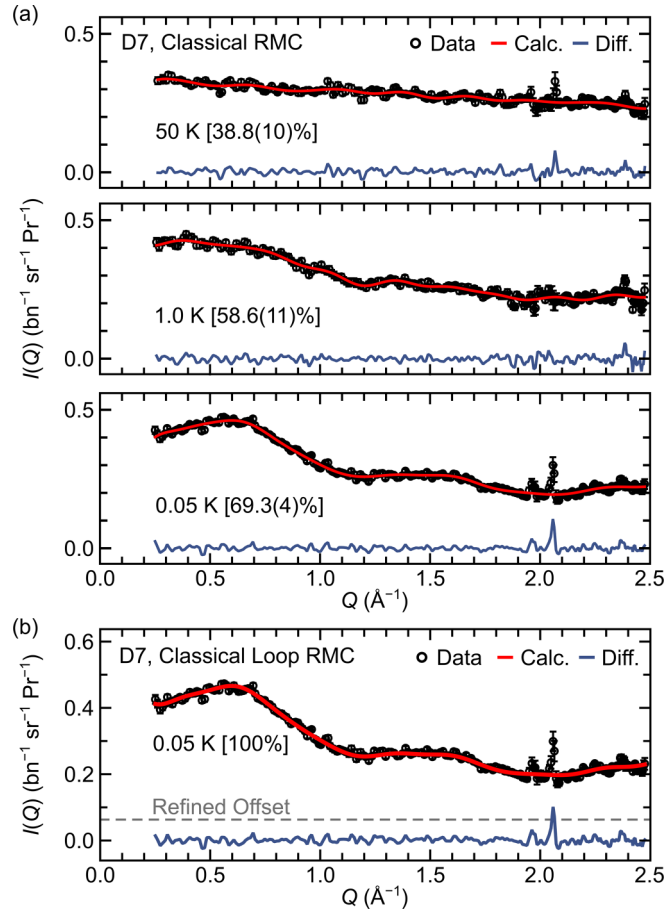


FIG. 6. (a) Comparison of the $Q$ dependence of the energy-integrated magnetic scattering for polycrystalline $Pr_2Sn_2O_7$ at various temperatures with the corresponding reverse Monte Carlo (RMC) fits as described in the text. Percentages denote the portion of tetrahedra that exhibit a two-in-two-out spin configuration. (b) Restricting the available parameter space to lie exclusively in the spin ice manifold for the RMC refinement cannot completely account for the differential magnetic cross section at 0.05 K. Instead, the model requires the addition of a $Q$-independent vertical offset.

temperature peak position in $C_{p,nm}$ and the minimum in the first derivative $dM/dH$, respectively. We have also identified the partial spin-freezing (SF) regime, demarcated by the peak position in the imaginary component of the ac susceptibility data (DR $\chi_{ac}$). Although this partial spin freezing may have an extrinsic origin as described above, it is notably absent in the field-polarized state. Tracking the field dependence of this feature arguably yields the best estimate of the critical field required for the suppression of the ice state, which is given by $\mu_0 H_c \sim 0.5$ T here. The fragility of the low-temperature, low-field spin ice state is reminiscent of previous work on the CSI systems $Dy_2Ti_2O_7$ and $Ho_2Ti_2O_7$ [79], as $\mu_0 H < 1$ T applied along the [001] direction was sufficient to generate an ordered spin ice state in those cases. The key features of the phase diagram, including the spin ice state, the low-temperature spin freezing, and the nature of the field-polarized phase are all hallmarks of a ferromagnetic Ising pyrochlore.

### D. Diffuse and inelastic neutron scattering

Finally, we conducted additional neutron scattering measurements to learn more about the properties of the ice state. Magnetic diffuse scattering was identified previously in polycrystalline $Pr_2Sn_2O_7$ with a $Q$ dependence that was indicative of spin-ice correlations [39]. While it was initially shown that a CSI model did not provide a complete description of the data, improved agreement between the data and theory was obtained by including the effect of quantum fluctuations in the latter [41,42]. We provide more insight into the nature of this magnetic diffuse scattering by presenting polarized neutron diffraction data from the D7 diffractometer that was analyzed with the reverse Monte Carlo (RMC) method. The results are summarized in Fig. 6. The RMC approach refines magnetic-moment $\boldsymbol{S}_i$ configurations directly to experimental data, without making any assumptions about the magnetic Hamiltonian [86,87]. Refinements were performed with the software SPINVERT [87] using $5 \times 5 \times 5$ supercells of the crystallographic unit cell and initialized with moment orientations randomly assigned as either parallel or antiparallel to the local $\langle 111 \rangle$ axes. At every iteration of a classical RMC refinement, a single spin is flipped, the goodness-of-fit is calculated according to Ref. [87] including a refined intensity scale factor, and the proposed spin flip is accepted or rejected according to the Metropolis algorithm. Refinements were converged until no further improvement in the fit was obtained. The choice of random initial configurations implies that the refined configurations are the most consistent with the experimental data and the assumption of Ising moments.

We performed two different types of refinements. The first method was classical RMC as described above with no additional constraints. Representative fitted curves are superimposed on the data in Fig. 6(a), with the percentage of tetrahedra obeying the ice rules at each temperature indicated on the panel. The ice correlations are significantly enhanced at low temperature as compared to expectations for a paramagnetic state, where $6/16 = 37.5\%$ of tetrahedra would follow the "two-in-two-out" ice rule by random chance. However, the 69.3(4)% fraction of tetrahedra obeying the ice rules at 0.05 K is well below the 100% CSI value. To check this result, the second refinement method ("classical loop RMC") constrained the spin configurations to remain entirely within the ice-rules manifold and fitted the data by using only "loop moves" that cycle between different ice-rules-obeying states [88]. The only way that the magnetic diffuse scattering data could be captured with a fully ice-rules-obeying state was to refine a constant intensity offset as well as an intensity scale factor. A representative fitted curve is superimposed on the 0.05 K data in Fig. 6(b), along with the value of this offset.

The indication of significant deviations from the ice rule at low temperature is surprising, since it is apparently inconsistent with our measurement of Pauling's zero-point entropy at low temperature. Since our polarized-neutron data should not include any appreciable contributions from nonmagnetic or background scattering, it is unlikely that the intensity offset in our classical loop RMC arises from these origins. Instead, it may be due to local quantum effects, which can cause fluctuations away from the ice-rules manifold. Since the RMC refinements consider magnetic moments as classical vectors, this potential origin is not distinguishable from thermally induced spin flips. Importantly, the D7 data represent integrated magnetic signals up to energy transfers of 3.5 meV. While this energy-integration range is not wide enough to capture the first crystal-field excitation at 17.8 meV [39,40], it integrates over the dispersionless magnetic excitations reported in [44], which were interpreted in terms of spatially confined emergent monopoles; i.e., deviations from the ice rule. Another possible explanation is that chemical disorder (e.g., $Pr^{4+}$ defects) could nucleate tetrahedra that do not obey the ice rule.

Neutron spectroscopy measurements obtained using the DCS instrument enable us to discriminate between the elastic and inelastic scattering features of the spin-ice state. Two experiments were performed with the same sample environment and $\lambda_n = 9$ Å; the base temperature was 0.20 K for Expt. 1 and and 0.02 K for Expt. 2. Except where otherwise noted, data were collected after cooling the sample in zero applied field. To remove background scattering, we subtracted data sets measured at base temperature in high applied magnetic fields (6 T for Expt. 1 and 9 T for Expt. 2). Our magnetic field-temperature phase diagram (Fig. 5) indicates that these parameter combinations place the sample deep within the field-polarized state, where magnetic scattering in the accessible energy range is localized to elastic magnetic Bragg peaks. Hence the background-subtracted signal away from the Bragg positions provides a good estimate of the purely magnetic scattering.

Figure 7(a) presents the $E$ dependence of the background-subtracted magnetic excitation spectrum at base temperature and in zero magnetic field. These data were integrated over a wide $Q$ range of [0.25, 0.95] $Å^{-1}$. The quasielastic scattering observed previously up to 0.3 meV energy transfers [39] that has been associated with confined magnetic monopoles [44] is apparent again here. The DCS data collected in Expt. 1 and Expt. 2 agree within statistical errors, confirming that these results are reproducible.

Figure 7(b) presents the $Q$ dependence of the energy-integrated and inelastic components of our base-temperature, zero-field DCS data. We estimated the energy-integrated scattering $I_{\text{tot}}(Q)$ by integrating $I(Q, E)$ over $[-0.17, 0.37]$ meV and the inelastic scattering $I_{\text{inel}}(Q)$ by integrating $I(Q, E)[1 + n(E)]$ over [0.014,0.37] meV, where $n(E)$ is the Bose factor. The lower bound of the latter integral was chosen because ∼93% of elastic scattering appears at energies below 0.014 meV.

These data were converted into absolute intensity units by normalizing to the Bragg intensity of the (111) nuclear peak. As a consistency check, we also plot our equivalently normalized D7 data as Expt. 3 in Fig. 7(b). The $Q$ dependence of the DCS data agrees well with the D7 data, except the overall intensity of the D7 data is slightly higher. This small discrepancy may be due to systematic errors in the normalization procedure or to the wider $E$-integration range of the D7 data, which extends to ∼3.5 meV and so may capture additional high-energy magnetic signals such as the dispersionless magnetic excitations reported in [44]. Notably, the energy dependence of the neutron data presented in Fig. 7(a) shows significant inelastic scattering at negative energy transfer (neutron energy gain), suggesting that the sample temperature was higher than the recorded temperature at the mixing chamber. Applying the detailed-balance law to the data shown in Fig. 7(a) indicates a sample temperature ∼0.5 K.

We compare the total magnetic moment with the dynamic magnetic moment using two different approaches. First, we calculate the magnetic moment directly from our neutron data as [89,90]

$$\mu_{\text{eff}}^2 = 3\left(\frac{2}{\gamma r_0}\right)^2 \frac{\int \frac{Q^2}{|f(Q)|^2} I(Q) dQ}{\int Q^2 dQ}, \tag{5}$$

where $(\frac{2}{\gamma r_0})^2$ is 13.77 sr $b^{-1}$, $f(Q)$ is the $Pr^{3+}$ isotropic magnetic form factor, and $\mu_{\text{eff}}$ is the magnetic moment. To obtain the total and dynamic moment, respectively $I(Q) = I_{\text{tot}}(Q)$ and $I_{\text{inel}}(Q)$ in Eq. (5). In principle, the integral in Eq. (5) runs over all $Q$, but in practice, it is necessary to restrict it to our usable $Q$ range of [0.25, 0.95] $Å^{-1}$. This approximation is justified here due to broadness of the magnetic scattering features. This approach provides a lower bound on the dynamic moment, since it assumes that all scattering within the elastic energy resolution of the data is purely elastic. As an alternative approach, we fit the energy dependence of our data (averaged over $Q$) to a sum of elastic (Gaussian) and quasielastic (Lorentzian) components,

$$I(E) = a_0 \exp\left(\frac{-E^2}{2\sigma^2}\right) + \frac{a_1}{1 - \exp(-E/k_B T)} \frac{E\Gamma}{E^2 + \Gamma^2}, \tag{6}$$

where $\Gamma$ is the fitted spin correlation rate, $a_0$ and $a_1$ are fitted parameters, $\sigma$ is the fixed energy resolution, and we take

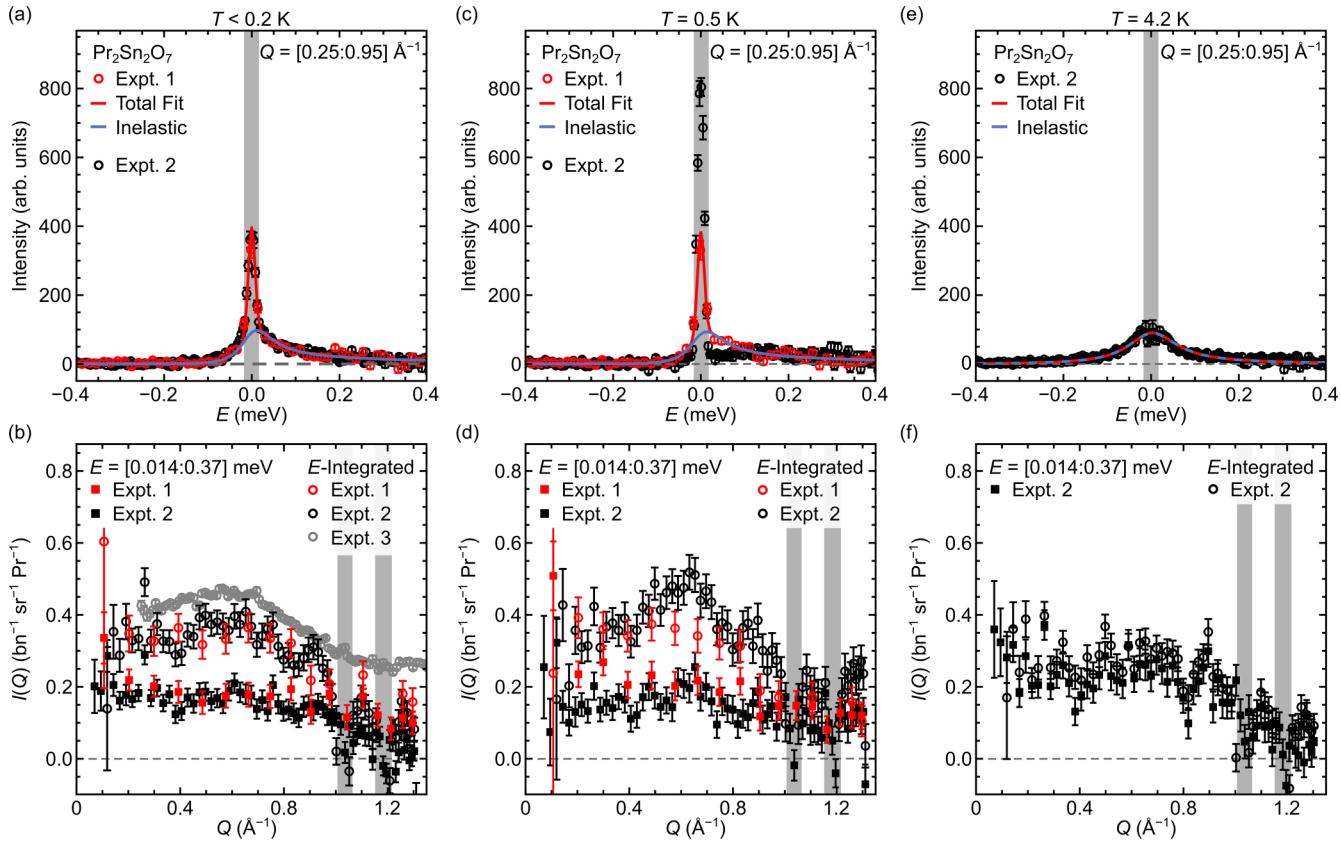


FIG. 7. (a) Intensity vs energy transfer $E$ integrated over a $Q$ range of [0.25, 0.95] Å$^{-1}$, measured after zero-field cooling at base temperature [$T = 0.20$ K for Expt. 1 (red circles); $T = 0.02$ K for Expt. 2 (black circles)]. The shaded gray region indicates the elastic portion of the spectrum. (b) Intensity vs momentum transfer $Q$ for energy-integrated data (empty circles) and inelastic data (filled squares). Data from experiments 1, 2, and 3 are labeled on the plots. For Expt. 1 and Expt. 2, energy integration ranges are $[-0.17, 0.37]$ meV and [0.014,0.37] meV for energy-integrated and inelastic data, respectively. For Expt. 3 (D7 data), energy integration extends to ∼3.5 meV. The shaded gray regions denote $Q$ regions affected by oversubtracted Bragg scattering. (c) Intensity vs $E$ measured in zero field at 0.5 K after zero-field cooling (Expt. 1, red circles) and at 0.5 K in zero field after a 0.02 K measurement in a 9 T field (Expt. 2, black circles), showing a strong dependence on magnetic-field history. (d) Intensity vs $Q$ for energy-integrated data (empty circles) and inelastic data (filled squares). Red symbols show data collected at 0.5 K after zero-field cooling (Expt. 1) and black symbols show data collected at 0.5 K in zero field after a 0.02 K measurement in a 9 T field. (e) Same as (a), except at 4.2 K. (f) Same as (b), except at 4.2 K and with integration range $[-0.37, 0.37]$ meV for the energy-integrated data.

$T = 0.5$ K at base temperature to match the observed ratio of the signal at negative vs positive energy transfer. The total and dynamic moments are proportional to the total and Lorentzian energy integrals, respectively, treating as dynamic the part of the Lorentzian curve that lies within the elastic line. All energy integrals are taken to a maximum energy of 0.37 meV.

An important quantity is the fraction of the magnetic spectral weight that is dynamic, $f_{\rm inel} \equiv (\mu_{\rm eff}^{\rm inel}/\mu_{\rm eff})^2$. Neglecting the effect of finite energy resolution, this fraction would be unity for a fully fluctuating state and $1/(J_{\rm eff}+1)$ for a fully ordered or frozen magnetic state with quantum number $J_{\rm eff}$. At 0.02 K, we find that at least 48(2)% of the magnetic spectral weight is dynamic, based on the lower bound described above. Fits to the energy dependence of the data estimate that 74(1)% of the spectral weight is contained in the Lorentzian (dynamic) peak shape. This value is greater than the 67% expected for a fully frozen state with $J_{\rm eff} = 1/2$ [91,92], but significantly less than the 100% expected for a fully dynamic state. Hence our base-$T$ neutron data are most consistent with a partially frozen ground state in the time scale probed by this technique. By contrast, a fully dynamic state is realized at 4.2 K, where the energy dependence is well described by the Lorentzian line shape only, with no Gaussian (elastic) contribution.

Our fits of Eq. (6) provide an estimate of the spin correlation time, which is obtained from the fitted relaxation rate as $\tau_{\rm neutron} = h/\Gamma \sim 10^{-10}$ s at base temperature (Table I). This time scale is much faster than the time scale extracted from our ac susceptibility measurements ($\sim 10^{-4}$ s), indicating the existence of distinct "fast" and "slow" time scales in the spin-ice regime [93]. The slow time scale identified by ac susceptibility is likely responsible for the magnetic spectral weight that lies within the elastic energy resolution of our DCS data.

Finally, we consider the dependence of the magnetic spectral weight on temperature and magnetic-field history. Our results are summarized in Table I. Neutron spectroscopy data collected at 0.5 K and 4.2 K are shown in Figs. 7(c)–7(f). The total moment obtained varies between 2.4 and 2.8 $\mu_{\rm B}$, in good agreement with the values obtained from bulk susceptibility

TABLE I. Values of the total magnetic moment $\mu_{\text{eff}}$, dynamic magnetic moment $\mu_{\text{eff}}^{\text{inel}}$, ratio $f_{\text{inel}} = (\mu_{\text{eff}}^{\text{inel}}/\mu_{\text{eff}})^2$, and fast spin correlation time $\tau_{\text{neutron}}$ obtained from inelastic neutron scattering data at different temperatures and for different magnetic-field histories. Temperatures denoted with an asterisk (*) are likely underestimates of the sample temperature, which we estimate as ∼0.5 K for these data sets. Values shown in *italics* were obtained from Expt. 1 and other values from Expt. 2 (see Fig. 7).

| $T$ (K) | Field history | $\mu_{\text{eff}}$ ($\mu_{\text{B}}$) | $\mu_{\text{eff}}^{\text{inel}}$ ($\mu_{\text{B}}$) | Min[$f_{\text{inel}}$] | $f_{\text{inel}}$ | $\tau_{\text{neutron}}$ (ns) |
|---|---|---|---|---|---|---|
| 0.02* | ZF | 2.61(3) | 1.80(3) | 0.48(2) | 0.74(1) | 0.102(4) |
| 0.2* | ZF | *2.52(7)* | *1.88(7)* | *0.55(5)* | 0.72(3) | 0.093(8) |
| 0.5 | ZF | *2.48(8)* | *1.97(8)* | *0.63(7)* | 0.73(3) | 0.087(8) |
| 4.2 | ZF | 2.37(3) | 2.14(4) | 0.82(4) | 1.0 | 0.061(2) |
| 0.5 | 9 T at 0.02 K | 2.82(4) | 1.79(5) | 0.40(2) | | |

and crystal-field analysis [40]. For the data collected under zero-field-cooling (ZFC) conditions, the dynamic fraction of spectral weight increases from at least 48(2)% at 0.02 K to at least 82(4)% at 4.2 K, consistent with increasing thermally induced spin flips. At 0.5 K only, data were collected with two different field histories. In Expt. 1, the protocol was ZFC to 0.2 K, measure, warm to 0.5 K, and measure the data shown in red in Figs. 7(c) and 7(d). In Expt. 2, the protocol was ZFC to 0.02 K, ramp field to 9 T, measure, ramp field to zero, warm to 0.5 K, and measure the data shown in black in Figs. 7(c) and 7(d). Interestingly, at 0.5 K, the field history of the sample has a significant effect on its magnetic excitation spectrum. For 0.5 K data from Expt. 1, the dynamic fraction of spectral weight is at least 63(7)%, but this fraction dramatically reduces to 40(2)% for data collected in Expt. 2. The low-energy ($E \lesssim 0.1$ meV) quasielastic scattering apparent in Expt. 1 appears to collapse to the elastic line in Expt. 2, while higher-energy inelastic scattering remains in Expt. 2. The strong dependence of the magnetic scattering on field history is consistent with the FC/ZFC splitting observed in our bulk magnetic susceptibility data [Fig. 2(c)] and is suggestive of glassy dynamics associated with partial spin freezing.

## IV. DISCUSSION

Our combined ac susceptibility, heat capacity, polarized neutron scattering, and neutron spectroscopy results paint an interesting picture of the spin ice state in $Pr_2Sn_2O_7$. Hallmarks of a homogeneous spin system with slow dynamics required for a CSI state are not apparent here, as the low-temperature drop in the real component of the ac susceptibility data and the nuclear Schottky peak amplitude in the heat capacity data are significantly suppressed as compared to expectations for a fully frozen spin system. These findings are corroborated by the reduced fraction of Pr tetrahedra obeying the ice rules at low temperature as revealed by the RMC analysis of our magnetic diffuse scattering data. Taken together, these results establish significant spin inhomogeneity with two main components. The slow component has spin correlation times on the order of $10^{-4}$–$10^{-3}$ s below ∼0.5 K, based on ac susceptibility measurements. The fast spin component has a spin correlation time on the order of $10^{-10}$ s at ∼0.5 K, based on fits to our neutron spectroscopy data. These results are in remarkably close agreement with theoretical calculations [93], which predict a bimodal distribution of spin correlation times that are of the same orders of magnitude we obtain experimentally. Importantly, the distinct "fast" and "slow" time scales we identify using ac susceptibility and neutron scattering are already present in the spin-ice phase at temperatures (∼0.5 K) above the partial spin-freezing transition at ∼0.25 K, and these two time scales also persist below the partial-spin-freezing transition. Therefore, we consider the presence of two time scales as a distinct phenomenon from the partial spin freezing. Our work suggests that $Pr_2Sn_2O_7$ has a partially frozen magnetic ground state, where the frozen spin fraction is likely nucleated by defects and/or disorder and may therefore be sample dependent. The rich landscape of possible dynamics in $Pr_2Sn_2O_7$ have been noted theoretically as well, with predictions suggesting a possibility of coherent many-body dynamics [93].

It is interesting to compare our results on $Pr_2Sn_2O_7$ to previous work on the other Pr pyrochlores. Of these, $Pr_2Zr_2O_7$ has received the most attention, likely due to the earliest availability of large single crystals. The initial samples were affected by structural disorder likely due to Pr off-centering or $Pr^{4+}$ defects [21]. On the one hand, these $Pr_2Zr_2O_7$ samples share some key features with our polycrystalline $Pr_2Sn_2O_7$ samples, including a partial spin freezing signature in ac susceptibility measurements and a nuclear Schottky amplitude much lower than expected for a fully frozen spin system [24]. On the other hand, the spin correlation time for the fast spin component in $Pr_2Zr_2O_7$ was shorter, as the total moment sum rule result obtained using 0.1 K neutron spectroscopy data revealed predominantly inelastic contributions in this case. The slower spin dynamics identified here in $Pr_2Sn_2O_7$ may be related to an enhanced amount of disorder and/or defects in the polycrystalline samples as compared to the early $Pr_2Zr_2O_7$ single crystals. Evidence for a dynamical ground state in $Pr_2Hf_2O_7$ has also been presented [29] despite complete [26] or partial spin freezing [27] signatures in ac susceptibility measurements, but unfortunately dilution fridge heat capacity measurements and a total moment sum rule analysis are not yet available to facilitate comparisons with our work. The collective results on the Pr pyrochlores continue to support their quantum spin ice candidacy, but point to sample-dependent defects and disorder as key issues that need to be better understood and quantified before their intrinsic properties can be revealed.

## V. CONCLUSIONS

We performed a detailed characterization study to investigate the low-temperature magnetic properties of the ferromagnetic Ising pyrochlore $Pr_2Sn_2O_7$. We first

identified key spin-ice signatures in our polycrystalline samples, including a ferromagnetic Curie-Weiss temperature, magnetic moments with Ising anisotropy, and the characteristic magnetic diffuse scattering pattern. Next, we established a magnetic field-temperature phase diagram for $Pr_2Sn_2O_7$ that includes all the characteristic features for a ferromagnetic Ising pyrochlore and shows that the spin ice state is sensitive to external perturbations with a critical field of only 0.5 T required to suppress it. Finally, we found important deviations from CSI physics that show the low-temperature magnetic state of $Pr_2Sn_2O_7$ is partially frozen with a dynamic component consisting of two different spin correlation times. More specifically, a finite ac susceptibility signal persists down to the base temperature of 60 mK and both the amplitude of the nuclear Schottky anomaly and the fraction of Pr tetrahedra obeying the ice rules are significantly reduced compared to expectations for CSI. It is likely that defect formation (e.g., $Pr^{4+}$) underlies the strong sample dependence in $Pr_2Sn_2O_7$. Regardless, our work suggests that $Pr_2Sn_2O_7$ remains a strong candidate to host a QSI ground state and calls for renewed efforts to characterize and control defects and disorder in Pr pyrochlores so the intimate connection between their chemistry and magnetic ground states can be definitively established.

## ACKNOWLEDGMENTS

B.R.O. (synthesis, bulk properties measurements and analysis), A.F.M. (bulk properties measurements), and J.A.M.P. (inelastic neutron scattering analysis, Monte Carlo simulations), gratefully acknowledge support from the U.S. Department of Energy (DOE), Office of Science, Basic Energy Sciences, Materials Sciences and Engineering Division. P.M.S. acknowledges additional financial support from the CCSF, RSC, ERC, and the University of Edinburgh through the GRS and PCDS. C.R.W. acknowledges financial support from the CRC (Tier II) program, CIFAR, CFI and NSERC. A portion of this research used resources at the High Flux Isotope Reactor, which is a DOE Office of Science User Facility operated by Oak Ridge National Laboratory. S.D.W., G.P., M.J.K., S.J.G.A., and P.M.S. acknowledge support from the U.S. Department of Energy (DOE), Office of Basic Energy Sciences, Division of Materials Sciences and Engineering under Grant No. DE-SC0017752. Neutron data collection [94] on the Diffuse Scattering Spectrometer D7 at the ILL took place with financial support from proposal 5-42-434 awarded to P.M.S. and C.R.W. A portion of this work used facilities supported via the UC Santa Barbara NSF Quantum Foundry funded via the Q-AMASE-i program under award DMR-1906325.

[1] L. Balents, Nature (London) **464**, 199 (2010).
[2] M. R. Norman, Rev. Mod. Phys. **88**, 041002 (2016).
[3] L. Savary and L. Balents, Rep. Prog. Phys. **80**, 016502 (2017).
[4] Y. Zhou, K. Kanoda, and T. K. Ng, Rev. Mod. Phys. **89**, 025003 (2017).
[5] J. Knolle and R. Moessner, Annu. Rev. Condens. Matter Phys. **10**, 451 (2019).
[6] H. Takagi, T. Takayama, G. Jackeli, G. Khaliullin, and S. E. Nagler, Nat. Rev. Phys. **1**, 264 (2019).
[7] J. Wen, S. L. Yu, S. Li, W. Yu, and J. X. Li, npj Quantum Mater. **4**, 12 (2019).
[8] C. Broholm, R. J. Cava, S. A. Kivelson, D. G. Nocera, M. R. Norman, and T. Senthil, Science **367**, eaay0668 (2020).
[9] J. R. Chamorro, T. M. McQueen, and T. T. Tran, Chem. Rev. **121**, 2898 (2021).
[10] S. T. Bramwell and M. J. P. Gingras, Science **294**, 1495 (2001).
[11] R. G. Melko and M. J. P. Gingras, J. Phys.: Condens. Matter **16**, R1277 (2004).
[12] C. Castelnovo, R. Moessner, and S. Sondhi, Annu. Rev. Condens. Matter Phys. **3**, 35 (2012).
[13] S. T. Bramwell and M. J. Harris, J. Phys.: Condens. Matter **32**, 374010 (2020).
[14] M. Udagawa and L. Jaubert, *Spin Ice* (Springer, New York, 2021).
[15] C. Castelnovo, R. Moessner, and S. L. Sondhi, Nature (London) **451**, 42 (2008).
[16] K. A. Ross, L. Savary, B. D. Gaulin, and L. Balents, Phys. Rev. X **1**, 021002 (2011).
[17] M. J. P. Gingras and P. A. McClarty, Rep. Prog. Phys. **77**, 056501 (2014).
[18] O. Benton, O. Sikora, and N. Shannon, Phys. Rev. B **86**, 075154 (2012).
[19] L. Savary and L. Balents, Phys. Rev. B **87**, 205130 (2013).
[20] M. C. Hatnean, C. Decorse, M. R. Lees, O. A. Petrenko, D. S. Keeble, and G. Balakrishnan, Mater. Res. Express **1**, 026109 (2014).
[21] S. M. Koohpayeh, J. J. Wen, B. A. Trump, C. L. Broholm, and T. M. McQueen, J. Cryst. Growth **402**, 291 (2014).
[22] M. C. Hatnean, R. Sibille, M. R. Lees, M. Kenzelmann, V. Ban, V. Pomjakushin, and G. Balakrishnan, J. Phys.: Condens. Matter **29**, 075902 (2017).
[23] V. K. Anand, A. T. M. N. Islam, A. Samartzis, J. Xu, N. Casati, and B. Lake, J. Cryst. Growth **498**, 124 (2018).
[24] K. Kimura, S. Nakatsuji, J. Wen, C. Broholm, M. Stone, E. Nishibori, and H. Sawa, Nat. Commun. **4**, 1934 (2013).
[25] P. Bonville, S. Guitteny, A. Gukasov, I. Mirebeau, S. Petit, C. Decorse, M. C. Hatnean, and G. Balakrishnan, Phys. Rev. B **94**, 134428 (2016).
[26] V. K. Anand, L. Opherden, J. Xu, D. T. Adroja, A. T. M. N. Islam, T. Herrmannsdörfer, J. Hornung, R. Schönemann, M. Uhlarz, H. C. Walker *et al.*, Phys. Rev. B **94**, 144415 (2016).
[27] R. Sibille, E. Lhotel, M. C. Hatnean, G. Balakrishnan, B. Fåk, N. Gauthier, T. Fennell, and M. Kenzelmann, Phys. Rev. B **94**, 024436 (2016).
[28] S. Petit, E. Lhotel, S. Guitteny, O. Florea, J. Robert, P. Bonville, I. Mirebeau, J. Ollivier, H. Mutka, E. Ressouche *et al.*, Phys. Rev. B **94**, 165153 (2016).
[29] R. Sibille, N. Gauthier, H. Yan, M. Ciomaga Hatnean, J. Ollivier, B. Winn, U. Filges, G. Balakrishnan, M. Kenzelmann, N. Shannon *et al.*, Nat. Phys. **14**, 711 (2018).

[30] N. Tang, Y. Gritsenko, K. Kimura, S. Bhattacharjee, A. Sakai, M. Fu, H. Takeda, H. Man, K. Sugawara, Y. Matsumoto *et al.*, Nat. Phys. **19**, 92 (2023).

[31] J.-J. Wen, S. M. Koohpayeh, K. A. Ross, B. A. Trump, T. M. McQueen, K. Kimura, S. Nakatsuji, Y. Qiu, D. M. Pajerowski, J. R. D. Copley *et al.*, Phys. Rev. Lett. **118**, 107206 (2017).

[32] K. Matsuhira, C. Sekine, C. Paulsen, M. Wakeshima, Y. Hinatsu, T. Kitazawa, Y. Kiuchi, Z. Hiroi, and S. Takagi, J. Phys.: Conf. Ser. **145**, 012031 (2009).

[33] J. P. Clancy, J. P. C. Ruff, S. R. Dunsiger, Y. Zhao, H. A. Dabkowska, J. S. Gardner, Y. Qiu, J. R. D. Copley, T. Jenkins, and B. D. Gaulin, Phys. Rev. B **79**, 014408 (2009).

[34] J. Snyder, B. G. Ueland, J. S. Slusky, H. Karunadasa, R. J. Cava, A. Mizel, and P. Schiffer, Phys. Rev. Lett. **91**, 107201 (2003).

[35] G. Ehlers, A. L. Cornelius, T. Fennell, M. Koza, S. T. Bramwell, and J. S. Gardner, J. Phys.: Condens. Matter **16**, S635 (2004).

[36] Y. Tokiwa, T. Yamashita, D. Terazawa, K. Kimura, Y. Kasahara, T. Onishi, Y. Kato, M. Halim, P. Gegenwart, T. Shibauchi *et al.*, J. Phys. Soc. Jpn. **87**, 064702 (2018).

[37] N. Martin, P. Bonville, E. Lhotel, S. Guitteny, A. Wildes, C. Decorse, M. Ciomaga Hatnean, G. Balakrishnan, I. Mirebeau, and S. Petit, Phys. Rev. X **7**, 041028 (2017).

[38] O. Benton, Phys. Rev. Lett. **121**, 037203 (2018).

[39] H. D. Zhou, C. R. Wiebe, J. A. Janik, L. Balicas, Y. J. Yo, Y. Qiu, J. R. D. Copley, and J. S. Gardner, Phys. Rev. Lett. **101**, 227204 (2008).

[40] A. J. Princep, D. Prabhakaran, A. T. Boothroyd, and D. T. Adroja, Phys. Rev. B **88**, 104421 (2013).

[41] S. Onoda and Y. Tanaka, Phys. Rev. Lett. **105**, 047201 (2010).

[42] S. Onoda and Y. Tanaka, Phys. Rev. B **83**, 094411 (2011).

[43] K. Matsuhira, C. Sekine, C. Paulsen, and Y. Hinatsu, J. Magn. Magn. Mater. **272-276**, E981 (2004).

[44] P. M. Sarte, A. A. Aczel, G. Ehlers, C. Stock, B. D. Gaulin, C. Mauws, M. B. Stone, S. Calder, S. E. Nagler, J. W. Hollett *et al.*, J. Phys.: Condens. Matter **29**, 45LT01 (2017).

[45] A. A. Coelho, J. Appl. Crystallogr. **51**, 210 (2018).

[46] K. Momma and F. Izumi, J. Appl. Crystallogr. **44**, 1272 (2011).

[47] S. Calder, K. An, R. Boehler, C. R. Dela Cruz, M. D. Frontzek, M. Guthrie, B. Haberl, A. Huq, S. A. J. Kimber, J. Liu *et al.*, Rev. Sci. Instrum. **89**, 092701 (2018).

[48] A. S. Wills, Phys. B: Condens. Matter **276-278**, 680 (2000).

[49] J. R. Stewart, P. P. Deen, K. H. Andersen, H. Schober, J.-F. Barthélémy, J. M. Hillier, A. P. Murani, T. Hayes, and B. Lindenau, J. Appl. Crystallogr. **42**, 69 (2009).

[50] O. Schärpf and H. Capellmann, Phys. Status Solidi A **135**, 359 (1993).

[51] G. Ehlers, J. R. Stewart, A. R. Wildes, P. P. Deen, and K. H. Andersen, Rev. Sci. Instrum. **84**, 093901 (2013).

[52] J. R. D. Copley and J. C. Cook, Chem. Phys. **292**, 477 (2003).

[53] M. Subramanian, G. Aravamudan, and G. Subba Rao, Prog. Solid State Chem. **15**, 55 (1983).

[54] B. J. Kennedy, B. A. Hunter, and C. J. Howard, J. Solid State Chem. **130**, 58 (1997).

[55] K. Matsuhira, Y. Hinatsu, K. Tenya, H. Amitsuka, and T. Sakakibara, J. Phys. Soc. Jpn. **71**, 1576 (2002).

[56] S. T. Bramwell, M. N. Field, M. J. Harris, and I. P. Parkin, J. Phys.: Condens. Matter **12**, 483 (2000).

[57] C. V. Topping and S. J. Blundell, J. Phys.: Condens. Matter **31**, 013001 (2019).

[58] K. Matsuhira, Y. Hinatsu, K. Tenya, and T. Sakakibara, J. Phys.: Condens. Matter **12**, L649 (2000).

[59] K. Matsuhira, Y. Hinatsu, and T. Sakakibara, J. Phys.: Condens. Matter **13**, L737 (2001).

[60] L. Pan, N. J. Laurita, K. A. Ross, B. D. Gaulin, and N. P. Armitage, Nat. Phys. **12**, 361 (2016).

[61] E. Gopal and E. Gopal, Specific Heats Low Temp. **1966**, 84 (1966).

[62] J. Hejtmánek, Z. Jirák, O. Kaman, K. Knížek, E. Šantavá, K. Nitta, T. Naito, and H. Fujishiro, Eur. Phys. J. B **86**, 305 (2013).

[63] D. Jin, H. Zhou, Y. Song, J. Luo, Y. Wang, T. Chen, X. Cai, X. Fan, Q. Ran, Z. Zhao *et al.*, Physica C **235-240**, 1751 (1994).

[64] A. K. Pathak, D. Paudyal, Y. Mudryk, K. A. Gschneidner, and V. K. Pecharsky, Phys. Rev. Lett. **110**, 186405 (2013).

[65] A. Sahling, P. Frach, and E. Hegenbarth, Phys. Status Solidi B **112**, 243 (1982).

[66] R. Movshovich, A. Yatskar, M. F. Hundley, P. C. Canfield, and W. P. Beyermann, Phys. Rev. B **59**, R6601 (1999).

[67] R. B. Adhikari, P. Shen, D. L. Kunwar, I. Jeon, M. B. Maple, M. Dzero, and C. C. Almasan, Phys. Rev. B **100**, 174509 (2019).

[68] R. D. Chirico, E. F. Westrum, Jr., J. B. Gruber, and J. Warmkessel, J. Chem. Thermodyn. **11**, 835 (1979).

[69] R. Mitarov, V. Tikhonov, L. Vasilev, A. Golubkov, and I. Smirnov, Phys. Status Solidi A **30**, 457 (1975).

[70] R. Vollmer, A. Faißt, C. Pfleiderer, H. v. Löhneysen, E. D. Bauer, P.-C. Ho, V. Zapf, and M. B. Maple, Phys. Rev. Lett. **90**, 057001 (2003).

[71] K. Matsuhira, M. Wakeshima, Y. Hinatsu, and S. Takagi, J. Phys. Soc. Jpn. **80**, 094701 (2011).

[72] J. Bauer, A. Hirsch, L. Bayarjargal, L. Peters, G. Roth, and B. Winkler, Chem. Phys. Lett. **654**, 97 (2016).

[73] J. Kondo, J. Phys. Soc. Jpn. **16**, 1690 (1961).

[74] B. Bleaney, J. Appl. Phys. **34**, 1024 (1963).

[75] A. Scheie, Exotic Magnetism in Frustrated Pyrochlore-Based Magnets, Ph.D. thesis, Johns Hopkins University, Baltimore, MD, 2019.

[76] O. V. Kovalev, *Representations of the Crystallographic Space Groups*, 2nd ed. (Gordon and Breach, Switzerland, 1993).

[77] A. M. Hallas, J. Gaudet, M. N. Wilson, T. J. Munsie, A. A. Aczel, M. B. Stone, R. S. Freitas, A. M. Arevalo-Lopez, J. P. Attfield, M. Tachibana *et al.*, Phys. Rev. B **93**, 104405 (2016).

[78] T. Fennell, O. A. Petrenko, G. Balakrishnan, S. T. Bramwell, J. D. M. Champion, B. Fak, M. J. Harris, and D. M. Paul, Appl. Phys. A **74**, S889 (2002).

[79] T. Fennell, O. A. Petrenko, B. Fåk, J. S. Gardner, S. T. Bramwell, and B. Ouladdiaf, Phys. Rev. B **72**, 224411 (2005).

[80] I. Mirebeau, A. Apetrei, J. Rodríguez-Carvajal, P. Bonville, A. Forget, D. Colson, V. Glazkov, J. P. Sanchez, O. Isnard, and E. Suard, Phys. Rev. Lett. **94**, 246402 (2005).

[81] K. Ueda, J. Fujioka, B. J. Yang, J. Shiogai, A. Tsukazaki, S. Nakamura, S. Awaji, N. Nagaosa, and Y. Tokura, Phys. Rev. Lett. **115**, 056402 (2015).

[82] Y. Yasui, Y. Kondo, M. Kanada, M. Ito, H. Harashina, M. Sato, and K. Kakurai, J. Phys. Soc. Jpn. **70**, 284 (2001).

[83] S. Singh, R. Suryanarayanan, R. Tackett, G. Lawes, A. K. Sood, P. Berthet, and A. Revcolevschi, Phys. Rev. B **77**, 020406(R) (2008).

[84] S. J. Gomez, P. M. Sarte, M. Zelensky, A. M. Hallas, B. A. Gonzalez, K. H. Hong, E. J. Pace, S. Calder, M. B. Stone, Y. Su *et al.*, Phys. Rev. B **103**, 214419 (2021).

[85] B. R. Ortiz, P. M. Sarte, G. Pokharel, M. Garcia, M. Marmolejo, and S. D. Wilson, Phys. Rev. Mater. **6**, 094403 (2022).

[86] J. A. M. Paddison and A. L. Goodwin, Phys. Rev. Lett. **108**, 017204 (2012).

[87] J. A. M. Paddison, J. R. Stewart, and A. L. Goodwin, J. Phys.: Condens. Matter **25**, 454220 (2013).

[88] A. M. Hallas, J. A. M. Paddison, H. J. Silverstein, A. L. Goodwin, J. R. Stewart, A. R. Wildes, J. G. Cheng, J. S. Zhou, J. B. Goodenough, E. S. Choi *et al.*, Phys. Rev. B **86**, 134431 (2012).

[89] P. M. Sarte, A. M. Arevalo-Lopez, M. Songvilay, D. Le, T. Guidi, V. Garcia-Sakai, S. Mukhopadhyay, S. C. Capelli, W. D. Ratcliff, K. H. Hong *et al.*, Phys. Rev. B **98**, 224410 (2018).

[90] P. M. Sarte, K. Cruz-Kan, B. R. Ortiz, K. H. Hong, M. M. Bordelon, D. Reig-i Plessis, M. Lee, E. S. Choi, M. B. Stone, S. Calder *et al.*, npj Quantum Mater. **6**, 42 (2021).

[91] K. A. Ross, J. W. Krizan, J. A. Rodriguez-Rivera, R. J. Cava, and C. L. Broholm, Phys. Rev. B **93**, 014433 (2016).

[92] K. W. Plumb, H. J. Changlani, A. Scheie, S. Zhang, J. W. Krizan, J. A. Rodriguez-Rivera, Y. Qiu, B. Winn, R. J. Cava, and C. L. Broholm, Nat. Phys. **15**, 54 (2019).

[93] B. Tomasello, C. Castelnovo, R. Moessner, and J. Quintanilla, Phys. Rev. Lett. **123**, 067204 (2019).

[94] https://doi.org/10.5291/ILL-DATA.5-42-434.